Electron and hole mobilities in bulk hematite from spin-constrained density functional theory

Christian S. Ahart,[†] Kevin M. Rosso,[*,‡] and Jochen Blumberger[*,†]

†*Department of Physics and Astronomy, University College London, London WC1E 6BT, UK*

‡*Pacific Northwest National Laboratory, Richland, Washington 99354, United States*

E-mail: kevin.rosso@pnnl.gov; j.blumberger@ucl.ac.uk

Abstract

Transition metal oxide materials have attracted much attention for photoelectrochemical water splitting, but problems remain, e.g. the sluggish transport of excess charge carriers in these materials, which is not well understood. Here we use periodic, spin-constrained and gap-optimised hybrid density functional theory to uncover the nature and transport mechanism of holes and excess electrons in a widely used water splitting material, bulk-hematite ($\alpha-Fe_2O_3$). We find that upon ionisation the hole relaxes from a delocalized band state to a polaron localised on a single iron atom with localisation induced by tetragonal distortion of the 6 surrounding iron-oxygen bonds. This distortion is responsible for sluggish hopping transport in the Fe-bilayer, characterised by an activation energy of 70 meV and a hole mobility of 0.031 cm^2/Vs. By contrast, the excess electron induces a smaller distortion of the iron-oxygen bonds resulting in delocalisation over two neighbouring Fe units. We find that 2-site delocalisation is advantageous for charge transport due to the larger spatial displacements per transfer step. As a result, the electron mobility is predicted to be a factor of 3 higher than the hole mobility, 0.098 cm^2/Vs, in qualitative agreement with experimental observations. This work provides new fundamental insight into charge carrier transport in hematite with implications for its photocatalytic activity.

1 Introduction

Understanding charge transport in transition metal oxides is essential to advancing technical frontiers across diverse fields ranging from biogeochemistry, to renewable energy materials and microelectronics. Hematite is a prominent example. It is a naturally abundant n-type semiconductor[1] and plays a crucial role in redox cycling,[2,3] bioremediation[4] and colloid chemistry.[5] Moreover, the mineral oxide has a visible spectrum band gap and consequently has attracted much interest as a photoanode material for water splitting,[6–11] although problems remain including low mobility and short carrier lifetimes.[12]

Given the large number of studies that this material has inspired over the past decades, it is noteworthy that the intrinsic electron and hole mobilities of undoped hematite remain experimentally poorly constrained. At the same time, ever improved computational methods are at our disposal to investigate charge transport. In particular, critical advances in the approximations used in density functional theory (DFT) enable ever increasing accuracy in describing the underlying physics controlling charge transport in this material.

At most practical temperatures, charge transport in hematite occurs through thermally-activated hopping of polarons, localised lattice distortions that lower the energy of the excess electron or hole such that it becomes self-trapped.[13] As hematite is a native n-type semiconductor and is frequently further doped with electron donors,[14–16] the electron polaron has received much greater attention and has been shown with both wavefunction[17–19] and density functional theory[15,20,21] methods to localise on Fe atoms via their 3d states. The nature of the electron hole polaron however appears to be more disputed, where some groups have shown that it localises on Fe atoms,[18] others on O atoms via 2p states[22,23] and one group even finding that there is no localised hole polaron.[15]

In the absence of conclusive experimental evidence[24,25] our previous work[26] sought to clarify this situation using the gap-optimised hybrid functional HSE06,[27] with large supercells under periodic boundary conditions, removing some of the complications and uncertainties present in earlier calculations. We have demonstrated that the electron hole polaron localises on a single iron atom, with octahedral distortion of the surrounding iron-oxygen bonds and a change in spin moment of $+0.66$, consistent with hybrid DFT[23] and Hartree-Fock[18] calculations from other groups. The electron polaron however delocalises equally across two neighbouring iron atoms as a consequence of the lower reorganisation energy for electrons compared to holes,[26] with a smaller change in spin moment of $+0.23$ over each iron atom.

In this paper we turn our attention to the calculation of electron and electron hole diffusivity and mobility for hematite. In particular, we would like to understand how the 2-site delocalised electron moves along the lattice and how its mobility differs from that of

the electron hole. Shown highlighted in Fig. 1 is a single antiferromagnetic (AFM) plane of hematite, referred to as an iron bilayer, where both the excess electron and excess hole may localise. We consider the mobility only within this basal plane, as electrical conductivity measurements show that conduction is four orders of magnitude greater than in the perpendicular direction.[28,29]

To this end, we calculate the electron transfer parameters and rates for electron and electron hole transfer in hematite using constrained density functional theory (CDFT). CDFT is an established method for generating diabatic electronic states and calculating ET parameters in molecular systems,[30–35] but applications to condensed phase/periodic systems remain rare to date. In previous related work we used a plane-wave implementation of CDFT to calculate ET parameters and rates for electron tunnelling between F-centre defects in MgO.[34] Though, applications to late (spin density rich) transition metal ions remained computationally prohibitive. In this work we take advantage of a recent and very efficient periodic atomic-orbital implementation of CDFT[36] to calculate at hybrid DFT level all the ET parameters required to predict the charge mobility of electrons and holes in bulk hematite. As with our previous work, we stress it is only due to the increasing efficiency of computer codes and platforms that it is possible to perform such expensive hybrid CDFT calculations in combination with large supercells.

We find that the hole polaron in hematite localises onto a single iron atom with tetragonal distortion of the six surrounding iron-oxygen bonds. The three-fold degenerate tetragonal distortion of the Fe octahedron is responsible for the low hole mobility in hematite, calculated as 0.031 cm^2/Vs, a property well recognised to bear directly upon the photocatalytic behaviour of hematite.[6,9] The higher mobility of the electron polaron, 0.098 cm^2/Vs, is attributed to a delocalisation over two neighbouring iron atoms, advantageous for charge transport due to the larger spatial displacements per transfer step.

The remainder of the paper is organised as follows. Section 2.1 presents a breakdown of the required electron transfer theory, with Section 3 detailing the computational methods

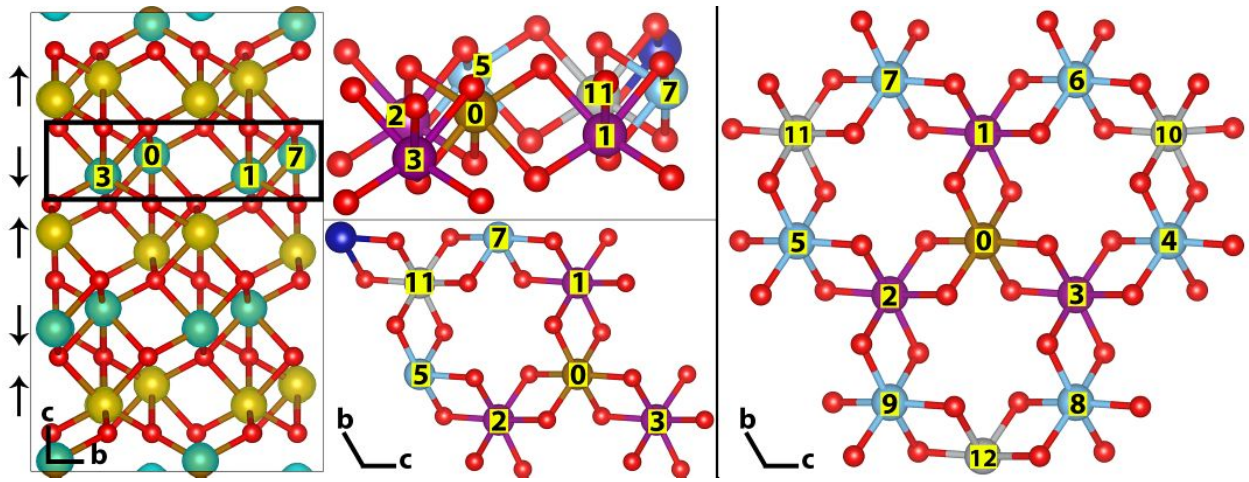

Figure 1: Structure of hematite. 2x2x1 supercell spin density (left), with a single AFM plane highlighted in black shown colour coded by distance from a central iron atom 0 (middle). A single AFM plane truncated to third nearest neighbours is shown (right). There are three first nearest neighbours (purple) at a distance of 2.97 Å, six second nearest neighbours (blue) at 5.04 Å and three third nearest neighbours (grey) at 5.87 Å. AFM spin orientation is indicated by arrows to the left of the figure.

used including details of the CDFT calculations. Section 4.1 presents the CDFT results for the hole polaron, Section 4.2 for the electron polaron and Section 4.3 the calculated mobilities. Section 5 presents a discussion of the results, and concluding remarks are made in Section 6.

2 Theory

2.1 Electron transfer theory

For calculation of the required ET parameters and mobility we adopt the same ET theory as used in previous studies of hematite,[18] and in other CDFT calculations.[34] The semi-classical expression for the rate of ET in a donor–acceptor complex derived from transition state theory in the harmonic approximation and Landau–Zener theory has the form[37,38]

$$k = \kappa_{\mathrm{el}} \nu_{\mathrm{n}} \exp\left(\frac{-\Delta A^{\ddagger}}{k_{\mathrm{B}} T}\right), \tag{1}$$

with the electronic transmission coefficient $\kappa_{\rm el} = 2P_{\rm LZ}/(1+P_{\rm LZ})$ where $P_{\rm LZ} = 1-\exp(-2\pi\gamma)$ is the Landau–Zener transition probability with γ the adiabaticity parameter defined as $2\pi\gamma = \pi^{3/2}\left\langle|H_{\rm ab}|^2\right\rangle_{\rm TS}/h\nu_{\rm n}\sqrt{\lambda k_{\rm B}T}$. $\left\langle|H_{\rm ab}|^2\right\rangle_{\rm TS}$ is the squared electronic coupling averaged over the transition state (TS) configurations, $\nu_{\rm n}$ is the effective nuclear frequency along the reaction coordinate, $\Delta A^{\ddagger}$ is the activation free energy, λ is the reorganization free energy, $k_{\rm B}$ the Boltzmann constant and T the temperature[39]. For an effective nuclear frequency we use the same value as Rosso and co-workers,[18] the energy of the highest infra-red active longitudinal optical mode phonon 1.85×10^{13} s^{-1}. We note this is very close to the experimental Fe-O stretch vibration 1.72×10^{13} s^{-1}.[40]

The general expression for the activation free energy $\Delta A^{\ddagger}$ valid in the non-adiabatic, adiabatic and intermediate regimes is[41]

$$\Delta A^{\ddagger} = A_0(\Delta E = 0) - A_0(\Delta E = \Delta E_0) \tag{2}$$

$$= \Delta A^{\ddagger}_{\rm na} - \Delta^{\ddagger}, \tag{3}$$

where A_0 is the free energy curve for the adiabatic electronic ground state for electron transfer taking the vertical energy gap, ΔE, as reaction coordinate,

$$\Delta E(\mathbf{R}^N) = E_b(\mathbf{R}^N) - E_a(\mathbf{R}^N), \tag{4}$$

E_a and E_b are the electronic energies for initial and final diabatic states a and b, $\mathbf{R}^N$ the nuclear configuration, $\Delta E = \Delta E_0$ the position of the minimum of state a and $\Delta E = 0$ the position of the TS.

$\Delta A^{\ddagger}_{\rm na}$ is the activation free energy on the diabatic electronic states

$$\Delta A^{\ddagger}_{\rm na} = \frac{(\lambda+\Delta A)^2}{4\lambda}, \tag{5}$$

and $\Delta^{\ddagger}$ is a correction that becomes important when the electronic coupling $H_{\rm ab}$ is large

$$\Delta^{\ddagger} = \left\langle |H_{\mathrm{ab}}|^2 \right\rangle_{\mathrm{TS}}^{1/2} - \frac{1}{\lambda} \left\langle |H_{\mathrm{ab}}|^2 \right\rangle_{\Delta E_0}, \tag{6}$$

with the assumption that the free energy difference, ΔA, between the initial and final state is zero, which is the case in hematite due to symmetry. Ignoring thermal effects of phonons on electronic coupling and reorganization free energy, the activation free energy is approximated by the activation energy, $\Delta E^{\ddagger}$

$$\Delta A^{\ddagger} \approx \Delta E^{\ddagger} = \frac{\lambda}{4} - (H_{\mathrm{ab}} - \frac{H_{\mathrm{ab}}^2}{\lambda}), \tag{7}$$

where H_{ab} is taken at the TS and the reorganisation energy λ is calculated as

$$\lambda = 4(E_a(TS) - E_a(\Delta E_0)), \tag{8}$$

where $E_a(TS)$ and $E_a(\Delta E_0)$ are the electronic energies of the initial diabatic state at the transition state and minimum energy nuclear configurations, respectively, calculated using CDFT. Note that for the current system, $E_a(\Delta E_0)$ is virtually identical with the DFT (adiabatic) ground state energy at the minimum energy nuclear configuration.

Charge transport in hematite can be modelled as a succession of hopping between sites, with associated rate constants calculated from Eq. 1. The corresponding charge mobility is obtained from the Einstein relation

$$\mu = \frac{eD}{k_{\mathrm{B}}T}. \tag{9}$$

Calculation of the diffusion coefficient D can be performed through methods such as kinetic Monte Carlo,[42] or by solving a chemical master equation to obtain the time-dependent charge population of each site as by Giannini et al.[43] The mean squared displacement (MSD) is calculated from the time evolution of the charge population, and following an initial non-linear equilibration period the diffusion coefficient is given by gradient of the MSD[44]

$$D = \frac{1}{2} \lim_{t \to \infty} \frac{d\mathrm{MSD}(t)}{dt}. \tag{10}$$

As a result of the lattice symmetry, diffusion is isotropic within the basal plane and therefore the calculated mobility tensor becomes a single value.

Alternatively, the diffusion coefficient can be calculated analytically for a 1D chain model as

$$D = \frac{R^2 i k}{2}, \tag{11}$$

for the transfer distance R, site multiplicity i and rate constant k. Rosso and co-workers[17,18] directly used Equation 11 for a 1D model of the 2D basal plane of hematite, with the site multiplicity i=3 to approximately account for the 3 first nearest neighbours of an iron atom in the 2D plane. Adelstein et al.[20] also used Equation 5 for an approximation of the 2D plane, but with i=0.5. Our approach moves beyond these approximations, calculating the full mobility tensor in the basal plane.

3 Computational methods

We use the range-separated hybrid functional HSE06,[27] with the percentage of exact Hartree-Fock exchange (HFX) modified to 12% to reproduce the experimental band gap of hematite.[45,46] In previous work we demonstrated that the standard definition of HSE06 with 25% HFX overestimates the experimental band gap of 2.2 eV as 3.6 eV,[47] and does not satisfy the generalised Koopmans condition.[26]

Initial coordinates were taken from the experimental crystal structure for hematite,[48] with geometry optimisation converged until the residual forces were smaller than 0.02 eV/Å. For a more complete discussion of the structure and setup of bulk hematite refer to Ref 23. The only change in this work was that the planewave cutoff was tightened from 400 to 600

Ry to aid in the verification of degenerate structures.

We find that the Hirshfeld spin moment on the Fe atom is a suitable descriptor for the polaronic states. The spin moment changes from -3.95 to -3.29 for the electron hole and -3.95 to -3.72 for each of the two Fe atoms over which the electron polaron is delocalized. Interestingly, the change in charge is not found to be a useful descriptor due to (paired) electron rearrangement, as also noted by other groups.[20,23]

For electron hole transfer between two Fe atoms, Fe_A and Fe_B, we define the initial (final) ET state as the spin constrained CDFT state with the spin moment on Fe_A (Fe_B) constrained to -3.29. For electron transfer between two 2-site delocalized Fe pairs, $(Fe_1\text{-}Fe_2)_A$ and $(Fe_3\text{-}Fe_4)_B$ we define the initial (final) ET state as the spin constrained CDFT state with the spin moment on each of the two iron atoms Fe_1 and Fe_2 (Fe_3 and Fe_4) constrained to -3.72. These constraints ensure that for any geometry (including transition state geometry) diabatic states are obtained that resemble very closely the DFT electronic ground state of the electron hole or electron polaron in the global minimum energy structure.

Other definitions of the spin constraint would be possible. For instance, one could include the first shell oxygen atoms but we found that their spin moment is rather small and their inclusion in the constraint is not beneficial. Moreover, one could constrain the spin density difference between donor and acceptor groups which is a common choice in CDFT calculations.[34] However, we found that a single absolute spin constraint on the Fe atoms in question is the most suitable choice in the present case.

To setup the CDFT calculations, first the polaron is localised on each of the desired iron atoms, typically by offsetting the local Fe-O bond lengths to encourage polaron formation at this location. After geometry optimisation to form the charged DFT ground state, linear interpolation is performed to create the transition state geometries. These transition state geometries are then used to calculate both the electronic couplings and reorganisation energies (Eq. 8) using CDFT. This is performed by constraining the spin moment of the iron atoms to the spin moment of the charged ground state given above, thus generating the

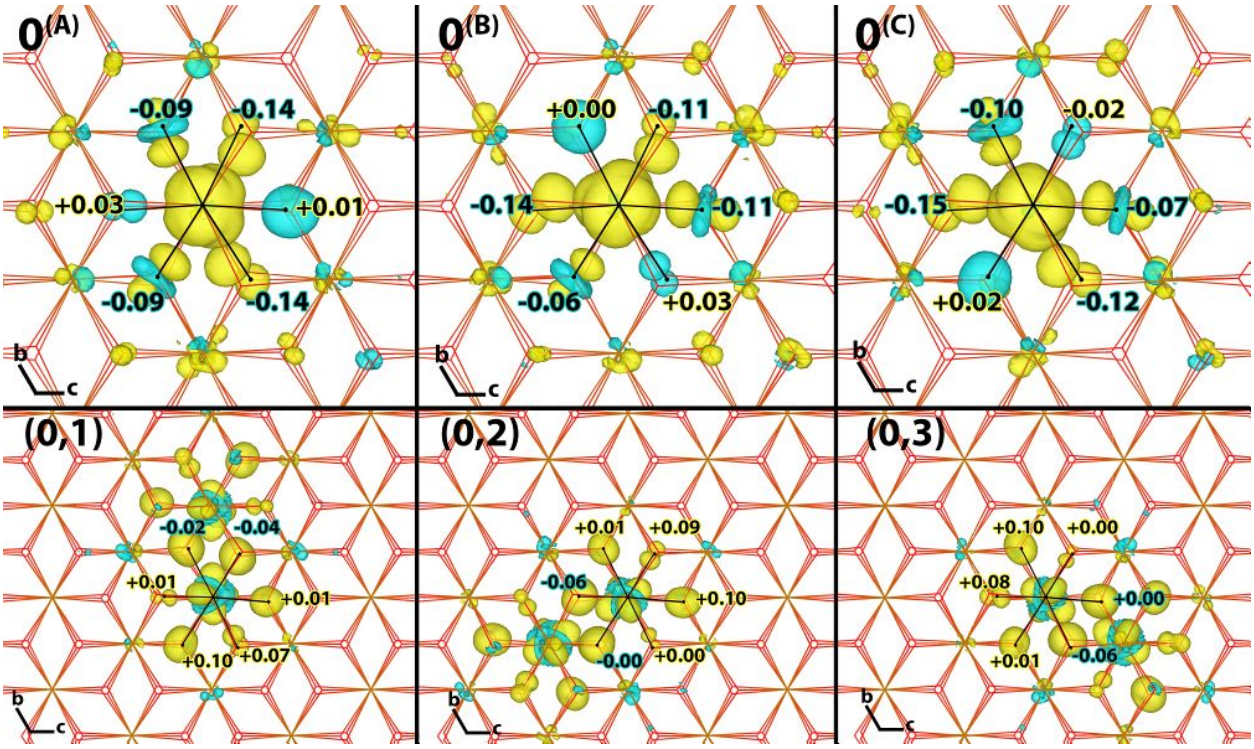

Figure 2: Excess hole and excess electron in hematite. 4x4x1 supercell excess spin density for ground state hole polaron (top) and electron polaron (bottom). A hole polaron localised on an iron atom has three degenerate structures (A, B and C) due to the octahedral distortion of the Fe-O bonds. As the electron polaron is localised across two iron atoms, for any combination of first nearest neighbours (A, B and C) the structures are also degenerate. Bond lengths between the iron atom and bonded oxygen atoms are shown in Angstrom.

diabatic electronic states at the transition state geometry.

4 Results

4.1 Hole polaron

The electron hole polaron, shown in Figure 2 (upper row) is mainly localised on a single Fe atom and to a lesser extent on 1st shell oxygen atoms. It is stabilised by an octahedral distortion of the iron-oxygen bonds. There is a contraction of four equatorial Fe-O bonds, and and a very slight expansion of two axial Fe-O bonds. These changes in bond lengths are in response to the removal of electron density in the equatorial plane, more specifically

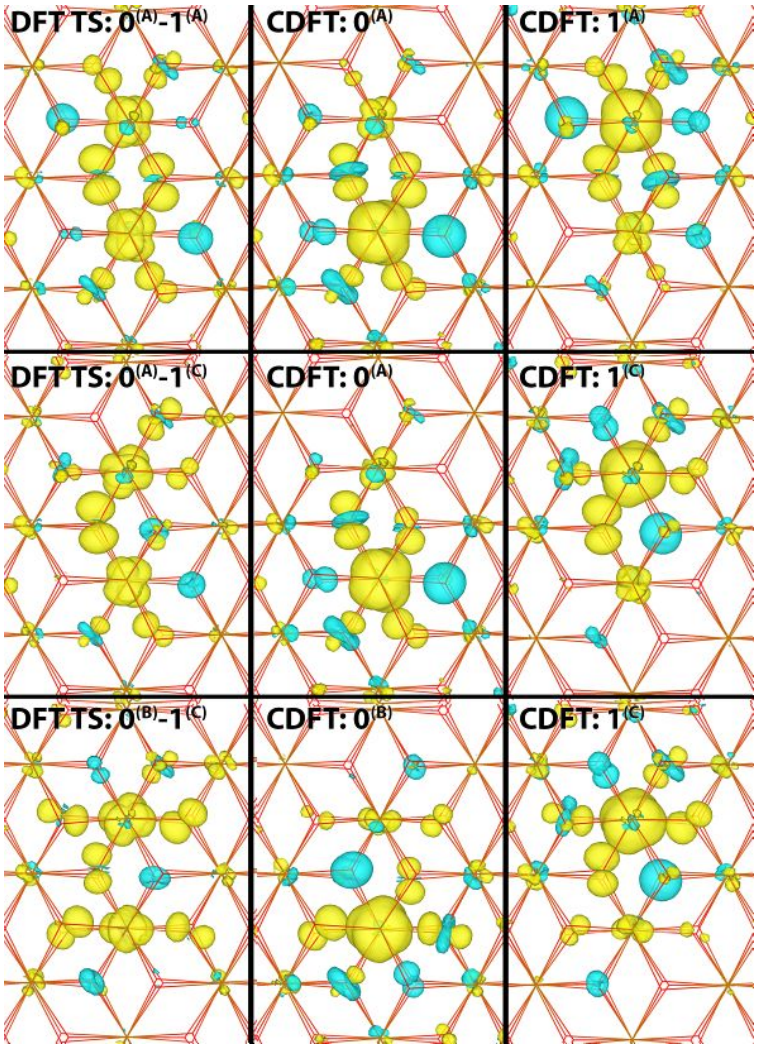

Figure 3: Excess hole transition states. 4x4x1 supercell excess spin density for DFT hole transition state (left column), with a spin constraint on atom 0 (middle column) and with a spin constraint on atom 1 (right column). Comparison with Fig. 2 reveals that the use of CDFT approximately reproduces the diabatic polaronic state on the transition state geometry. Refer to Fig. 1 for atom labelling.

in response to removal of an electron from a $d_{x^2-y^2}$ orbital. Similar tetragonal elongation is observed in the Jahn-Teller effect of high spin d^4 complexes, however this is not strictly Jahn-Teller distortion as there are there are two distinct groups of Fe-O bond lengths of 1.94 and 2.12 Å in the neutral geometry due to the iron bilayer. [48]

Importantly, we find that in the hematite lattice, the tetragonally distorted structure can be realised in three equivalent ways giving exactly the same electronic energy, see Figure 2 (upper row). Each of these symmetry-related structures can be transformed into one

Table 1: First nearest neighbour electronic coupling for the hole polaron in bulk hematite, accounting for all possible degenerate structures of atoms 0 and 1. All other atom combinations can be inferred by symmetry, e.g. highest coupling direction $0^{(A)}1^{(A)}$ is equivalent to $0^{(B)}2^{(B)}$.

Electronic coupling / meV			
	$1^{(A)}$	$1^{(B)}$	$1^{(C)}$
$0^{(A)}$	203	110	101
$0^{(B)}$	110	53	39
$0^{(C)}$	101	39	53

another by lattice vibrations. To the best of our knowledge this three-fold degeneracy of the hole polaron has not been previously explored, and its effect on the mobility has not been investigated.

Due to the 3-fold structural degeneracy, there are 3 x 3 = 9 possible transition state structures for hole transfer between an Fe atom and any of the three nearest neighbours. However, only 5 of these 9 combinations are unique featuring different donor-acceptor orbital combination and electronic coupling, see Table 1, and reorganisation and activation energy, Table 2. Note that the same set of 5 unique electronic couplings exist for all 3 nearest neighbours.

The 5 unique nearest neighbour couplings can be placed into three groups shown in Fig. 3: highest coupling (203 meV) where the polaron in initial and final ET states has $d_{x^2-y^2}$ orbitals aligned along the Fe-Fe direction shown in Fig. 3 (upper row); moderate coupling (101, 110 meV) where in one polaronic state the $d_{x^2-y^2}$ orbital is aligned along the Fe-Fe direction shown in Fig. 3 (middle row); low couplings (39, 53 meV) where in neither polaronic state the $d_{x^2-y^2}$ orbital is aligned along the Fe-Fe direction shown in Fig. 3 (lower row). The reorganisation energies of the 5 unique combinations are also slightly different, all ET parameters and rates are summarised in Table 2.

Similar considerations apply for second nearest neighbours and beyond. However, as accounting for every structural combination of the hole polaron for all of the second and third nearest neighbours would become too computationally demanding, we choose to only

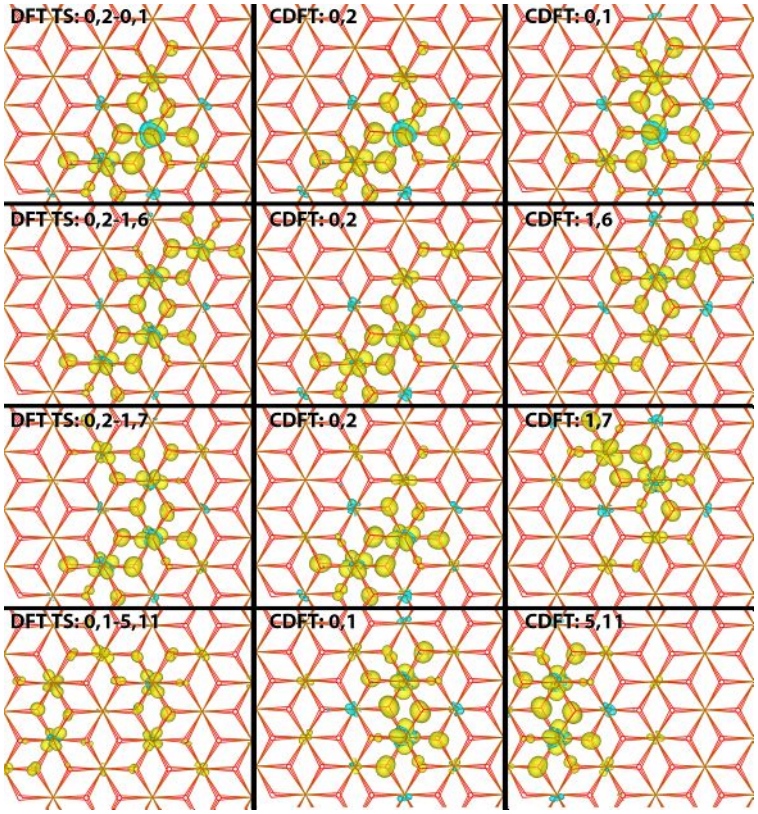

Figure 4: Excess electron transition states. 4x4x1 supercell excess spin density for DFT electron transition state (left column), with a spin constraint on region 1 (middle column) and with a spin constraint on region 2 (right column). Comparison with Fig. 2 reveals that the use of CDFT approximately reproduces the diabatic polaronic state on the transition state geometry. Refer to Fig. 1 for atom labelling. While the DFT localisation of the polaron on the transition state is asymmetric, the symmetry of the transition state structure can be qualitatively confirmed from inspection of the neutral DFT LUMO (see ESI).

consider these for the (A) orientation of the hole polaron. As Table 2 shows, the decay of the electronic coupling with distance and the increase in reorganisation energy is such that the interaction of the hole polaron with its second and third nearest neighbours is negligible. This means that only nearest neighbour charge transfer processes are important for the hole polaron in bulk hematite, consistent with work from other groups.[17,18]

4.2 Electron polaron

In previous work we found that the excess electron in hematite is delocalised over two neighbouring iron sites in the DFT electronic ground state.[26] According to electron transfer

theory, this suggests that electronic coupling between 1-site localised excess electronic states is so large that they are are no longer stable states, that is, they no longer correspond to a minimum of the ground state potential energy surface. This is the case as soon as $H_{\mathrm{ab}} > \frac{\lambda}{2}$.[41] We are now in a position to further verify this hypothesis using CDFT.

Indeed, using CDFT to constrain the excess electron on a single Fe atom, we obtain a very large coupling value of 407 meV (4x4x1 supercell), while an upper limit for reorganisations energy for nearest neighbour hopping of the 1-site localised electron polaron can be estimated to be 0.49 eV,[26] hence $H_{\mathrm{ab}} > \frac{\lambda}{2}$. Thus, both DFT calculation of the electronic ground state (adiabatic representation) and CDFT calculations of spin-localised states (diabatic representation) suggest that the 1-site localised electron polaron is unstable and delocalises over 2 adjacent sites.

Considering a given iron atom "0", delocalisation can occur over one of the three first nearest neighbours of 0: either (0,1); (0,2) or (0,3) (see Fig. 2 for numbering scheme). These states are energy degenerate due to the symmetry of the lattice. There are several possible charge transfer events of 2-site delocalized electron polaron. The shortest transfer (2.97 Å between centres of excess spin) includes the transitions: (0,1)-(0,2); (0,1)-(0,3) and (0,2)-(0,3) where (0,1)-(0,2) denotes the electron transfer from the 2-site delocalized state (0,1) to the 2-site delocalized state (0,2), and similarly for the other electron transfers. All of these three electron transfers are equivalent by symmetry. The coupling between these adjacent states is surprisingly small given that they share an Fe atom with significant excess spin density in both states. The reason is that the Fe t2g orbital carrying the excess spin density is rotated by 120 degrees with respect to one another in the two diabatic electronic states, see Figure 4 (upper row). This results in a small overlap of the two (non-orthogonal) diabatic CDFT electronic wavefunctions and thus a small electronic coupling.

Transfers over the next largest distances (5.04 Å between the centres of excess spin) includes the transitions: (0,2)-(1,6), (0,2)-(1,7) and (0,1)-(5,11) as shown in Fig. 4. The highest coupling is found for combination (0,2)-(1,6) where the iron t2g orbitals which the

excess electron occupies are orientated parallel. While the combination (0,1)-(5,11) has the same centre of mass distance, the iron atoms do not share Fe-O bonds as for the other two transition states and as such the coupling is the lowest of the three.

4.3 Electron hole and electron mobilities

The three structurally degenerate states of the hole polaron are expected to interconvert fast, on the time scale of the high frequency lattice modes ($\sim 10^{13}$ s^{-1}). This allows us to perform a Boltzmann average over the electronic couplings and reorganisation energy for the 9 possible transitions i, with weights proportional to $\exp(-\beta\lambda_i/4)$, and use the averages for calculation of a nearest neighbour hopping rate (Eq. 1). The latter is $\sim 10^{12}$, slow enough to support degenerate mixing of hole states by phonons. The rates for second and third nearest neighbour hops are orders of magnitudes smaller showing that only first nearest neighbour hops are important for hole polaron transport.

Table 3 gives the hole mobility for bulk hematite in the 2D (Fe bilayer) plane at room temperature, calculated by solving a chemical master equation to get the MSD and diffusion coefficient (Eq. 10) as by Giannini et al.[43] Inclusion of the six second nearest neighbours and three third nearest neighbours of the hole polaron increases the mobility only from 3.08×10^{-2} to 3.10×10^{-2} cm^2/Vs. To the best of our knowledge this is the first calculation of a mobility tensor in hematite, which fully accounts for the effect of the 2D conduction environment.

We have also examined finite size effects for the hole polaron, finding that the smaller 2x2x1 supercell commonly used in the literature provides both an underestimate of the electronic couplings and an overestimate of the reorganisation energy and therefore a lower mobility. This is attributed to the smaller reorganisation of the first coordination shell ('inner sphere') in the larger supercell (see ESI for more details).

For the electron polaron, we consider both the three transitions over the shortest possible distance and the transition over the next largest distance having the highest electronic cou-

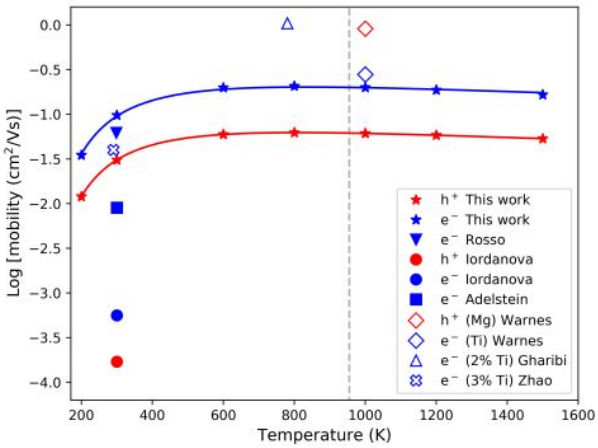

Figure 5: Mobility as a function of temperature. Literature calculated mobilities indicted with solid filled markers, doped experimental mobilities as unfilled markers. Our results are valid below the Neel temperature (T=955 K),[49] indicated with a dashed line. See ESI for an alternate plot where literature calculated mobilities are re-calculated using Equations 1-9.

pling. Due to the 2-site delocalised electron polaron structure, there are only four symmetry related second nearest neighbours to which the polaron may hop (see ESI Figure 5). This introduces a similar complication to the hole polaron, that for a single energy degenerate structure of the electron polaron the mobility is locally anisotropic. As there are three energy degenerate structures for a given electron polaron, the overall mobility remains isotropic. The electron mobility calculated for hopping to first nearest neighbours is 2.0×10^{-2} cm^2/Vs while for second nearest neighbours is 7.8×10^{-2} cm^2/Vs, as a consequence of how the coupling for first nearest neighbours is smaller than for second nearest neighbours due to unfavourable orientation of orbitals. Combining both first and second nearest neighbour mobility gives a total mobility of 9.8×10^{-2} cm^2/Vs. Hops across larger distances are not expected to contribute to electron mobility as the electronic coupling for those decays very quickly.

5 Discussion

Table 3 shows a comparison of our calculated and literature results, with Figure 5 showing this comparison plotted as mobility against temperature. A direct comparison of different

Table 2: Summary of ET parameters. Coupling, reorganisation energy, activation energy, transmission coefficient and rate constant for bulk hematite at room temperature. For the hole polaron the Boltzmann average for the electronic coupling and reorganisation energy is calculated for each nearest neighbour, while for the electron polaron there is only a single second nearest neighbour with an adiabaticity parameter greater than one and therefore this is not necessary.

r / Å	Neighbour	H_{ab} (meV)	λ (meV)	$\Delta E^{\ddagger}$ (meV)	κ_{el}	k (s^{-1})
Hole polaron						
2.97	$0^{(A)}$-$1^{(A)}$	203	652	23	1.0	7.5×10^{12}
	$0^{(A)}$-$1^{(B)}$	110	814	108	1.0	2.8×10^{11}
	$0^{(A)}$-$1^{(C)}$	101	784	108	1.0	2.8×10^{11}
	$0^{(B)}$-$1^{(B)}$	53	865	166	0.9	2.5×10^{10}
	$0^{(B)}$-$1^{(C)}$	39	881	183	0.7	1.1×10^{10}
	Average	147[a]	752[b]	70	1.0	1.2×10^{12}
5.04	$0^{(A)}$-$4^{(A)}$	15	1050	248	0.2	2.2×10^{8}
	$0^{(A)}$-$5^{(A)}$	8	1050	255	0.1	5.3×10^{7}
	$0^{(A)}$-$6^{(A)}$	15	1028	242	0.2	2.8×10^{8}
	$0^{(A)}$-$7^{(A)}$	30	1016	225	0.5	1.5×10^{9}
	$0^{(A)}$-$8^{(A)}$	28	1022	228	0.5	1.2×10^{9}
	$0^{(A)}$-$9^{(A)}$	16	1034	243	0.2	3.0×10^{8}
	Average	21[a]	103[b]	237	0.3	5.7×10^{8}
5.87	$0^{(A)}$-$10^{(A)}$	3	1087	269	0.0	4.4×10^{6}
	$0^{(A)}$-$11^{(A)}$	9	1106	268	0.1	3.9×10^{7}
	$0^{(A)}$-$12^{(A)}$	45	1026	213	0.8	3.6×10^{9}
	Average	32[a]	1061[b]	234	0.5	1.1×10^{9}
Electron polaron						
2.97	(0,1)-(0,2)	26	363	67	0.6	8.0×10^{11}
5.04	(0,2)-(1,6)	57	522	80	0.9	7.7×10^{11}
	(0,2)-(1,7)	19	572	125	0.3	4.9×10^{10}
	(0,1)-(5,11)	10	641	150	0.1	5.7×10^{9}

[a] Boltzmann average for electronic coupling $H_{ab} = \left(\sum_i H_{ab,i}^2 e^{\frac{-\lambda_i}{4k_B T}} / \sum_i e^{\frac{-\lambda_i}{4k_B T}} \right)^{\frac{1}{2}}$ for hole transition states i, see ESI for further detail.

[b] Boltzmann average for reorganisation energy $\lambda = 4 \left(\sum_i \frac{\lambda_i}{4} e^{\frac{-\lambda_i}{4k_B T}} / \sum_i e^{\frac{-\lambda_i}{4k_B T}} \right)$ for hole transition states i, see ESI for further detail.

mobility calculations is difficult due to the different methods used, and therefore we alleviate this somewhat by comparing to mobilities obtained according to Equations 1-9 using the reported literature values for electronic couplings and reorganisation energy.

Rosso and co-workers[17,18] performed Hartree-Fock calculations of both hole and electron mobility for small hematite clusters, considering up to second nearest neighbours. Both

Table 3: Summary of results and comparison with literature. To facilitate direct comparison, both the mobility cited in the paper (μ_{lit}) as well as mobilities re-calculated using Equations 1-9 for the 2D plane (μ_{2D}) are provided. Literature results are presented in chronological ordering by method.

Source	Dopant	H_{ab} (meV)	λ (meV)	$\Delta A^{\ddagger}$ (meV)	T (K)	μ_{lit} (cm^2/Vs)	μ_{2D} (cm^2/Vs)
Hole polaron							
This work		147	752	70	300		3.1×10^{-2}
This work		147	752	70	1000		6.1×10^{-2}
Cluster HF[18]		200	1590	220	298	1.7×10^{-4}	8.3×10^{-5}
Estimate[50]				100	300	1×10^{-2}	
Experiment[51]	Mg			200	1000	9.1×10^{-1}[a]	
Electron polaron							
This work		57	522	80	300		9.8×10^{-2}
This work		57	522	80	1000		2.0×10^{-1}
Cluster HF[17]		200	1200	110	298	6.2×10^{-2}	2.6×10^{-3}
Cluster HF[18]		190	1420	190	298	5.6×10^{-4}	2.9×10^{-4}
Bulk DFT[20]		41	(674)[b]	130	300	9.0×10^{-3}	1.4×10^{-3}
Bulk DFT[21]		40	800	(162)[b]	300		6.2×10^{-4}
Estimate[50]				100	300	1×10^{-2}	
Experiment[52]	Nb, Zr				960-1500	1×10^{-1}	
Experiment[51]	Ti			170	1000	2.8×10^{-1}[a]	
Experiment[53]	2%Ti			80	780	2×10^{-2}	
Experiment[54]	3%Ti			118	290	4×10^{-2}	
Experiment[54]	5%Ti			116	290	4.6×10^{-1}	
Experiment[54]	9%Ti			116	290	1.4×10^{-1}	

[a] Calculated from fitted mobility equation given in paper, valid above 923 K.

[b] Calculated in this work from values in paper.

their couplings and reorganisation energies tend to be considerably higher resulting in larger activation energies and lower mobilities for both electrons and holes. Though, one early estimate reported by Rosso and co-workers[17] for electron mobility is within a factor of 1.6 of our current best estimate. In previous work[26] we attributed the larger reorganisation energy of cluster models to the absence of lattice strain effects present in the bulk structure, as well as the use of Hartree-Fock which tends to overbind excess charge.

Adelstein et al.[20] and Behara et al.[21] calculated electron mobilities using a similar periodic supercell approach as in this work but with DFT+U in place of hybrid CDFT to model the polaronic states. Their reorganisation energies are similar, albeit slightly higher than ours and significantly smaller than typical values for cluster models. In fact, Behara reported values for bulk hematite around half of that for the 1D chain.[21] Their electronic coupling

values are also very similar to our estimates but this is a coincidence as our electronic polaronic states are 2-site delocalized whereas theirs are localised on a single iron atom. The 2-site delocalisation also permits larger transfer distances for a single hop resulting in higher mobilities than the 1-site localised polaron (see R^2 dependence, Eq. 11). This is partly the reason for the higher electron mobilities that we obtain in this current work compared to Adelstein et al. and Behara et al. Interestingly, Adelstein et al. in their calculations did find that there was some degree of delocalisation of the electron polaron over two iron atoms, identified from both a shorter Fe-Fe bond length and from the magnetic moment.

While other groups have attempted a justification of their results via comparison to experiment, this is problematic as there are no experimental results for the mobility of pure (undoped) hematite. The available experimental mobilities are all for doped hematite, sometimes for temperatures above the Neel temperature where hematite is no longer antiferromagnetic (955 K).[49] Further, as there are no direct measurements of either the reorganisation energy or couplings there are multiple combinations of each that would compare well with the observed mobilities.

The most suitable experimental data for comparison are probably the ones reported by Zhao et al[54] for electron mobility in 3% and 5% Ti-doped hematite. These values are within a factor of 2.5 of our computed mobilities for pure hematite, which is reassuring despite the above mentioned caveats.

6 Conclusion

In this work both the electron and hole mobility has been calculated for hematite using spin-constrained gap-optimised hybrid density functional theory with large supercells. Where previous studies have only considered coupling between a single nearest neighbour or a single orientation of the polaron, we account for all possible degenerate polaron structures and coupling with up to third nearest neighbours. In addition, for the first time the mobility

is calculated for the full 2D Fe bilayer rather than for a 1D model.

The CDFT calculations reported herein provide further evidence that the excess electron is delocalized over two iron sites and hops across the hematite crystal as a two-site delocalized polaron. While the activation energy for these hops is slightly higher, the hopping distance is larger than for the 1-site localised hole polaron. As a consequence, the electron mobility is predicted to be a factor of 3 higher than the hole mobility.

Charge transport has been identified as a key issue for the use of hematite in a number of technological applications, especially in photocatalysis and photoelectrochemistry.[6,9,11,12] Our study provides a comprehensive and detailed understanding of the physical mechanisms that lead to the sluggish transport of charge carriers in bulk hematite. This sets the scene for similar calculations at the hematite/liquid water interface, for which we have recently carried out *ab-initio* molecular dynamics simulations.[55,56] In particular, it will be important to understand if and how the presence of water at the interface changes the picture obtained for the bulk material and how this depends on the specific surface cut under investigation and the protonation state of the surface.[57] Such investigations, which the current work has now made possible, could help refine models, and resolve ongoing questions, about rate-limiting transport processes governing photocatalytic water splitting efficiency at hematite/water interfaces.[11,12] Work towards this goal is currently being carried out in our laboratory.

We have shown in this work that CDFT is a useful tool for the prediction of charge mobilities in an ubiquitous oxide material. The method is generally applicable to semiconducting materials and may be applied to other oxides of technological interest for the study of intrinsic charge transfer processes or for charge transfer between defects. Moreover, the CDFT approach is well suited for the study of interfacial charge transfer processes between different semiconductors or between semiconductor electrodes and liquids. It could thus become an essential tool for the emerging field of *ab-initio* electrochemistry.

Acknowledgement

C.A would like to thank Samuele Giannini for their assistance with calculation of the mobility tensor. C.A. gratefully acknowledges a PhD studentship cosponsored by University College London and Pacific Northwest National Laboratory (PNNL) through its BES Geosciences program supported by the U.S. Department of Energy's Office of Science, Office of Basic Energy Sciences, Chemical Sciences, Geosciences and Biosciences Division. Via our membership of the UK's HEC Materials Chemistry Consortium, which is funded by EPSRC (EP/L000202, EP/R029431), this work used the ARCHER UK National Supercomputing Service (http://www.archer.ac.uk), as well as the UK Materials and Molecular Modeling (MMM) Hub, which is partially funded by EPSRC (EP/P020194), for computational resources.

Supporting Information Available

The Supporting Information is available free of charge

- Finite size effects of electronic coupling and reorganisation energy, electronic coupling from alternative methods, details of Boltzmann average of electronic coupling and reorganisation energy, images of electron and hole polaron, schematic describing polaron hopping scheme, mobility with re-calculated literature values, correlation between overlap and electronic coupling, details of CDFT code (PDF)

References

(1) Dare-Edwards, M.; Goodenough, J.; Hamnett, A.; Trevelick, P. Electrochemistry and Photoelectrochemistry of Iron(III) Oxide. *J. Chem. Soc., Faraday Trans. I* **1983**, *79*, 2027–2041.

(2) Vargas, M.; Kashefi, K.; Blunt-Harris, E. L.; Lovley, D. R. Fe (III) reduction on early Earth. *Nature* **1998**, *395*, 65–67.

(3) Eggleston, C. M. Geochemistry: Toward new uses for hematite. *Science.* **2008**, *320*, 184–185.

(4) Braunschweig, J.; Bosch, J.; Meckenstock, R. U. Iron oxide nanoparticles in geomicrobiology: From biogeochemistry to bioremediation. *N. Biotechnol.* **2013**, *30*, 793–802.

(5) Philippe, A.; Schaumann, G. E. Interactions of dissolved organic matter with natural and engineered inorganic colloids: A review. *Environ. Sci. Technol.* **2014**, *48*, 8946–8962.

(6) Sivula, K.; Le Formal, F.; Grätzel, M. Solar water splitting: Progress using hematite (α-Fe 2O3) photoelectrodes. *ChemSusChem* **2011**, *4*, 432–449.

(7) Valdés, A.; Brillet, J.; Grätzel, M.; Gudmundsdóttir, H.; Hansen, H. A.; Jónsson, H.; Klüpfel, P.; Kroes, G. J.; Le Formal, F.; Man, I. C.; Martins, R. S.; Nørskov, J. K.; Rossmeisl, J.; Sivula, K.; Vojvodic, A.; Zäch, M. Solar hydrogen production with semiconductor metal oxides: New directions in experiment and theory. *Phys. Chem. Chem. Phys.* **2012**, *14*, 49–70.

(8) Xu, S.; Carter, E. A. Theoretical Insights into Heterogeneous (Photo)electrochemical CO2 Reduction. *Chem. Rev.* **2019**, *119*, 6631–6669.

(9) Wang, Q.; Domen, K. Particulate Photocatalysts for Light-Driven Water Splitting: Mechanisms, Challenges, and Design Strategies. *Chem. Rev.* **2020**, *120*, 919–985.

(10) Deleuze, P.-M.; Magnan, H.; Barbier, A.; Silly, M.; Domenichini, B.; Dupont, C. Unraveling the Surface Reactivity of Pristine and Ti-Doped Hematite with Water. *J. Phys. Chem. Lett.* **2021**, *12*, 11520–11527.

(11) Li, J.; Chen, H.; Triana, C. A.; Patzke, G. R. Hematite Photoanodes for Water Oxidation: Electronic Transitions, Carrier Dynamics, and Surface Energetics. *Angew. Chemie - Int. Ed.* **2021**, *60*, 18380–18396.

(12) Grave, D. A.; Yatom, N.; Ellis, D. S.; Toroker, M. C.; Rothschild, A. The "Rust" Challenge: On the Correlations between Electronic Structure, Excited State Dynamics, and Photoelectrochemical Performance of Hematite Photoanodes for Solar Water Splitting. *Adv. Mater.* **2018**, *30*, 1706577.

(13) Biswas, S.; Wallentine, S.; Bandaranayake, S.; Baker, L. R. Controlling polaron formation at hematite surfaces by molecular functionalization probed by XUV reflection-absorption spectroscopy. *J. Chem. Phys.* **2019**, *151*, 104701.

(14) Liao, P.; Toroker, M. C.; Carter, E. A. Electron transport in pure and doped hematite. *Nano Lett.* **2011**, *11*, 1775–1781.

(15) Lee, J.; Han, S. Thermodynamics of native point defects in α-Fe2O3: An ab initio study. *Phys. Chem. Chem. Phys.* **2013**, *15*, 18906–18914.

(16) Smart, T. J.; Ping, Y. Effect of defects on the small polaron formation and transport properties of hematite from first-principles calculations. *J. Phys. Condens. Matter* **2017**, *29*, 394006.

(17) Rosso, K. M.; Smith, D. M.; Dupuis, M. An ab initio model of electron transport in hematite (α-Fe2O3) basal planes. *J. Chem. Phys.* **2003**, *118*, 6455–6466.

(18) Iordanova, N.; Dupuis, M.; Rosso, K. M. Charge transport in metal oxides: A theoretical study of hematite α-Fe2O3. *J. Chem. Phys.* **2005**, *122*, 144305.

(19) Bylaska, E. J.; Rosso, K. Corresponding Orbitals Derived from Periodic Bloch States for Electron Transfer Calculations of Transition Metal Oxides. *J. Chem. Theory Comput.* **2018**, *14*, 4416–4426.

(20) Adelstein, N.; Neaton, J. B.; Asta, M.; De Jonghe, L. C. Density functional theory based calculation of small-polaron mobility in hematite. *Phys. Rev. B - Condens. Matter Mater. Phys.* **2014**, *89*, 245115.

(21) Behara, P. K.; Dupuis, M. Electron transfer in extended systems: characterization by periodic density functional theory including the electronic coupling. *Phys. Chem. Chem. Phys.* **2019**, *22*, 10609–10623.

(22) Liao, P.; Carter, E. A. Hole transport in pure and doped hematite. *J. Appl. Phys.* **2012**, *112*, 013701.

(23) Ansari, N.; Ulman, K.; Camellone, M. F.; Seriani, N.; Gebauer, R.; Piccinin, S. Hole localization in Fe2 O3 from density functional theory and wave-function-based methods. *Phys. Rev. Mater.* **2017**, *1*, 035404.

(24) Gardner, R. F.; Sweett, F.; Tanner, D. W. The electrical properties of alpha ferric oxide-I. The impure oxide. *J. Phys. Chem. Solids* **1963**, *24*, 1175–1181.

(25) Braun, A.; Sivula, K.; Bora, D. K.; Zhu, J.; Zhang, L.; Grätzel, M.; Guo, J.; Constable, E. C. Direct observation of two electron holes in a hematite photoanode during photoelectrochemical water splitting. *J. Phys. Chem. C* **2012**, *116*, 16870–16875.

(26) Ahart, C. S.; Blumberger, J.; Rosso, K. M. Polaronic structure of excess electrons and holes for a series of bulk iron oxides. *Phys. Chem. Chem. Phys.* **2020**, *22*, 10699–10709.

(27) Krukau, A. V.; Vydrov, O. A.; Izmaylov, A. F.; Scuseria, G. E. Influence of the exchange screening parameter on the performance of screened hybrid functionals. *J. Chem. Phys.* **2006**, *125*, 224106.

(28) Nakau, Electrical conductivity of Fe2O3. *J. Phys. Soc. Japan* **1960**, *15*, 727–727.

(29) Benjelloun, D.; Bonnet, J. P.; Doumerc, J. P.; Launay, J. C.; Onillon, M.; Hagenmuller, P. Anisotropie des proprietes electriques de l'oxyde de fer Fe2O3α. *Mater. Chem. Phys.* **1984**, *10*, 503–518.

(30) Wu, Q.; Van Voorhis, T. Extracting electron transfer coupling elements from constrained density functional theory. *J. Chem. Phys.* **2006**, *125*, 164105.

(31) Kaduk, B.; Kowalczyk, T.; Van Voorhis, T. Constrained density functional theory. *Chem. Rev.* **2012**, *112*, 321–370.

(32) de la Lande, A.; Salahub, D. R. Derivation of interpretative models for long range electron transfer from constrained density functional theory. *J. Mol. Struct. THEOCHEM* **2010**, *943*, 115–120.

(33) McKenna, K. P.; Blumberger, J. Crossover from incoherent to coherent electron tunneling between defects in MgO. *Phys. Rev. B - Condens. Matter Mater. Phys.* **2012**, *86*, 245110.

(34) Blumberger, J.; McKenna, K. P. Constrained density functional theory applied to electron tunnelling between defects in MgO. *Phys. Chem. Chem. Phys.* **2013**, *15*, 2184–2196.

(35) Kubas, A.; Gajdos, F.; Heck, A.; Oberhofer, H.; Elstner, M.; Blumberger, J. Electronic couplings for molecular charge transfer: Benchmarking CDFT, FODFT and FODFTB against high-level ab initio calculations. II. *Phys. Chem. Chem. Phys.* **2015**, *17*, 14342–14354.

(36) Holmberg, N.; Laasonen, K. Efficient Constrained Density Functional Theory Implementation for Simulation of Condensed Phase Electron Transfer Reactions. *J. Chem. Theory Comput.* **2017**, *13*, 587–601.

(37) Newton, M. Electron Transfer Reactions in Condensed Phases. *Annu. Rev. Phys. Chem.* **1984**, *35*, 437–480.

(38) Newton, M. D. Quantum Chemical Probes of Electron-Transfer Kinetics: The Nature of Donor-Acceptor Interactions. *Chem. Rev.* **1991**, *91*, 767–792.

(39) Blumberger, J. Recent Advances in the Theory and Molecular Simulation of Biological Electron Transfer Reactions. *Chem. Rev.* **2015**, *115*, 11191–11238.

(40) Santos, A. F.; Macedo, L. J.; Chaves, M. H.; Espinoza-Castañeda, M.; Merkoçi, A.; Limac, F. D. C. A.; Cantanhêde, W. Hybrid self-assembled materials constituted by ferromagnetic nanoparticles and tannic acid: A theoretical and experimental investigation. *J. Braz. Chem. Soc.* **2016**, *27*, 727–734.

(41) Spencer, J.; Scalfi, L.; Carof, A.; Blumberger, J. Confronting surface hopping molecular dynamics with Marcus theory for a molecular donor-acceptor system. *Faraday Discuss.* **2016**, *195*, 215–236.

(42) Wu, F.; Ping, Y. Combining Landau-Zener theory and kinetic Monte Carlo sampling for small polaron mobility of doped BiVO4 from first-principles. *J. Mater. Chem. A* **2018**, *6*, 20025–20036.

(43) Giannini, S.; Carof, A.; Blumberger, J. Crossover from Hopping to Band-Like Charge Transport in an Organic Semiconductor Model: Atomistic Nonadiabatic Molecular Dynamics Simulation. *J. Phys. Chem. Lett.* **2018**, *9*, 3116–3123.

(44) Oberhofer, H.; Reuter, K.; Blumberger, J. Charge Transport in Molecular Materials: An Assessment of Computational Methods. *Chem. Rev.* **2017**, *117*, 10319–10357.

(45) Pozun, Z. D.; Henkelman, G. Hybrid density functional theory band structure engineering in hematite. *J. Chem. Phys.* **2011**, *134*, 1–9.

(46) Elmaslmane, A. R.; Watkins, M. B.; McKenna, K. P. First-Principles Modeling of Polaron Formation in TiO2 Polymorphs. *J. Chem. Theory Comput.* **2018**, *14*, 3740–3751.

(47) Sherman, D. M. Electronic structures of iron(III) and manganese(IV) (hydr)oxide minerals: Thermodynamics of photochemical reductive dissolution in aquatic environments. *Geochim. Cosmochim. Acta* **2005**, *69*, 3249–3255.

(48) Maslen, E. N.; Streltsov, V. A.; Streltsova, N. R.; Ishizawa, N. Synchrotron X-ray study of the electron density in α-Fe2O3. *Acta Crystallogr. Sect. B Struct. Sci.* **1994**, *50*, 435–441.

(49) Lu, H. M.; Meng, X. K. Neel Temperature of Hematite Nanocrystals. *J. Phys. Chem.* **2010**, *114*, 21291–21295.

(50) Morin, F. Electrical Properties of alpha Fe2O3. *Phys. Rev.* **1954**, *93*, 1195–1199.

(51) Warnes, B. M.; Aplan, F. F.; Simkovich, G. Electrical conductivity and seebeck voltage of Fe2O3, pure and doped, as a function of temperature and oxygen pressure. *Solid State Ionics* **1984**, *12*, 271–276.

(52) Van Daal, H. J.; Bosman, A. J. Hall effect in CoO, NiO, and α-Fe2O3. *Phys. Rev.* **1967**, *158*, 736–747.

(53) Gharibi, E.; Hbika, A.; Dupre, B.; Gleitzer, C. Electrical Properties of Pure and Titanium-Doped Hematite Single Crystals, in the Basal Plane, at Low Oxygen Pressure. *Eur. J. Solid State Inorg. Chem.* **1990**, *27*, 647–658.

(54) Zhao, B.; Kaspar, T. C.; Droubay, T. C.; McCloy, J.; Bowden, M. E.; Shutthanandan, V.; Heald, S. M.; Chambers, S. A. Electrical transport properties of Ti-doped Fe2O3 (0001) epitaxial films. *Phys. Rev. B* **2011**, *84*, 245325.

(55) Von Rudorff, G. F.; Jakobsen, R.; Rosso, K. M.; Blumberger, J. Fast Interconversion of Hydrogen Bonding at the Hematite (001)-Liquid Water Interface. *J. Phys. Chem. Lett.* **2016**, *7*, 1155–1160.

(56) McBriarty, M. E.; Von Rudorff, G. F.; Stubbs, J. E.; Eng, P. J.; Blumberger, J.; Rosso, K. M. Dynamic Stabilization of Metal Oxide-Water Interfaces. *J. Am. Chem. Soc.* **2017**, *139*, 2581–2584.

(57) Gittus, O. R.; Von Rudorff, G. F.; Rosso, K. M.; Blumberger, J. Acidity Constants of the HematiteLiquid Water Interface from Ab Initio Molecular Dynamics. *J. Phys. Chem. Lett.* **2018**, *9*, 5574–5582.

TOC Graphic

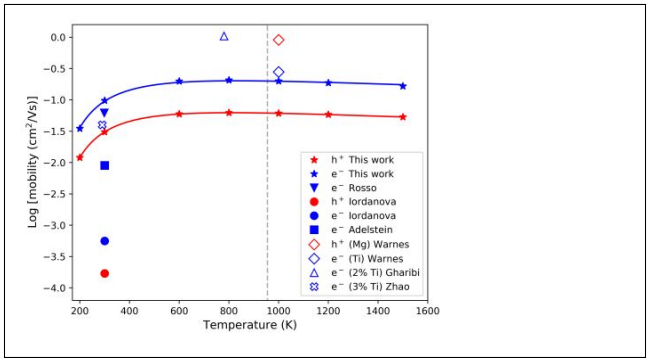
0.0
−0.5
−1.0
−1.5
−2.0
−2.5
−3.0
−3.5
−4.0
Log [mobility (cm²/Vs)]
200
400
600
800
1000
1200
1400
1600
Temperature (K)
h⁺ This work
e⁻ This work
e⁻ Rosso
h⁺ Iordanova
e⁻ Iordanova
e⁻ Adelstein
h⁺ (Mg) Warnes
e⁻ (Ti) Warnes
e⁻ (2% Ti) Gharibi
e⁻ (3% Ti) Zhao